PAPER

Investigation of the afterpeaks in pulsed microwave argon plasma at atmospheric pressure

View the article online for updates and enhancements.

You may also like

Investigation of the afterpeaks in pulsed microwave argon plasma at atmospheric pressure

Seokyong Jeong[1] (iD)**, Woojin Nam**[1,3] (iD)**, Seungbo Shim**[3] **and Gunsu Yun**[1,2,*] (iD)

[1] Physics, Pohang University of Science and Technology, 77, Cheongam-ro, Nam-gu, Pohang, Gyeongsangbuk-do, 37673, Republic of Korea
[2] Division of Advanced Nuclear Engineering, Pohang University of Science and Technology, 77, Cheongam-ro, Nam-gu, Pohang-si, Pohang, Gyeongsangbuk-do, 37673, Republic of Korea
[3] Mechatronics Research, Samsung Electronics Co., Ltd, 1, Samsungjeonja-ro, Hwaseong-si, gyeonggi-do 18448, Republic of Korea

E-mail: gunsu@postech.ac.kr

CrossMark

Abstract
We studied the energy transport process in pulsed microwave argon plasmas at atmospheric pressure, focusing on the optical emission burst during the pulse-off time called the afterpeak. Guided by experimental observations using nanosecond time resolution imaging and spectroscopic diagnostics, we developed a global simulation model considering time-varying reaction rate coefficients and non-thermal electron energy distribution. Experimental and simulation results show that the afterpeak can be maximized by choosing an appropriate pulse period. Our analysis of the generation and consumption of excited argon species reveals that the rapid drop in electron temperature during the inter-pulse time reduces the diffusive loss of ions and enhances the recombination reactions, which produce the afterpeak. We also reveal that the radiation trapping and high energy level argon must be considered to simulate the afterpeak in atmospheric conditions. The improved understanding of the afterpeak dynamics can be utilized to optimize the power coupling and/or generation of reactive species.

(Some figures may appear in colour only in the online journal)

1. Introduction

Pulsed-power-driven plasmas have several advantages over continuous-wave (CW) driven plasmas. Given the same average power, the instantaneous power at the pulse-on time is much higher, forming a short-lived high-density plasma [1]. The transient high-density plasma can be used as a source of electron beams [2, 3] and as a radiation source for x-ray lithography [4]. Mass spectroscopy using pulse-type glow discharge shows higher accuracy than the mass spectroscopy using CW plasma because, during the inter-pulse time, the ions in plasma bulk diffuse out while the ions are produced by Penning ionization, thus increasing the signal-to-noise ratio [5–7].

Pulse-driven plasmas can maintain a lower gas temperature, owing to heat loss during the inter-pulse time, than the gas temperature of CW plasmas with the same electron density. The power coupled to the plasma can become highly efficient at the rise of each pulse, producing energetic electrons [7] that are not typically generated in the CW operation. The low gas temperature and the transient high density of energetic electrons offer a unique chemical reaction environment, making the pulse-driven plasmas valuable and attractive for many practical applications such as hydrogen atom sources [8], NO_x decomposition [9, 10], and diamond deposition [11].

---

[*] Author to whom any correspondence should be addressed.

1361-6595/23/015003+12$33.00   Printed in the UK
1

In semiconductor etching processes, pulse operation is adopted so that the residual gas species can be removed in the inter-pulse duration, improving the stability and performance of etching [12]. In resonance-type plasma sources, pulse operation can minimize the impedance mismatching caused by uncontrolled variation of the plasma (load) impedance, enhancing power transmission efficiency [13].

Pulsed plasmas often show an afterglow, that is, light emission in the inter-pulse time. Afterglows can be classified into two types according to the power cut-off method: the flowing afterglow (FA) with a spatial division of the discharge and afterglow regions by the flow of the working gas, and the stationary afterglow (SA) with a temporal division of the discharge and afterglow times by turning off the power. The FA mode realizes a spatial separation of reaction zones, which helps measure the reaction coefficients of ion-involving reactions [14, 15] and synthesize nanoparticles [16]. The SA mode may be considered a realization of population inversion of excited states as in the laser pulse spectroscopy [17].

Under certain conditions, the afterglow appears as a peaked emission, and this type of afterglow has been termed afterpeak [18]. Several studies reported the afterpeak phenomena at various pressures. Yan *et al* [19] observed the time evolution of individual line emissions during the afterpeak in low pressure (few Torr) DC Ar–Cu glow discharge. Carbone *et al* [20] investigated the afterpeak of pulsed microwave-driven plasmas in a few hundred Torr. Chaplin and Bellan [21] presented a method to measure the unknown pressure by analyzing the observed afterpeak. Nam *et al* [22] investigated the time scales of the afterpeak in atmospheric pressure pulsed microwave plasmas for different pulse parameters, finding the optimal condition for the maximum afterpeak intensity. In numerical modeling of argon plasmas, Bogaerts [23] quantitatively verified that the dissociative recombination of the argon dimer ions is the leading cause of the afterpeak.

Hitherto, several researchers have studied the afterpeak either experimentally or theoretically [18–23]. However, detailed comparisons between the experimental observations and corresponding numerical simulations are rare in the available literature. In our previous experimental study on the afterpeak in the atmospheric pressure plasmas [22], we found that the recombination of argon dimer increases due to the rapid decrease of the electron temperature during pulse-off time, which is responsible for the afterpeak phenomena. In addition, we suggested that the generation of reactive species can be maximized by adjusting proper operation conditions, but specific conditions were not presented. Our previous study only presented a qualitative possibility for the occurrence of afterpeak but lacked quantitative analysis. This study aims to verify that afterpeak can occur at atmospheric pressure, using global modeling. In building a global model to reproduce afterpeak, we learned about physical phenomena, whose influence is underestimated in most fluid simulations despite having a substantial effect on the plasma chemistry in an atmospheric pressure environment.

The remainder of this paper is organized as follows. Section 2 describes the experimental setup designed to investigate the afterpeak in atmospheric pressure microwave plasmas and the global model containing the key reactions responsible for the afterpeak. Section 3 shows the experimental results and the numerical simulations and discusses the results. Section 3.1 summarizes the observations and simulation results, identifying the conditions to maximize the average light emission. We present the simulation result that reproduces the experimental result in section 3.2. While trying to build the simulation, we found that highly excited levels (HLs) and radiation trapping (RT) is essential for reproducing the afterpeak at atmospheric pressure. In section 3.3, we analyze the simulation results from the perspective of the reaction rates and the change in energy dissipation to identify the cause of the afterpeak. Further, section 3.4 discusses why the HLs and RT significantly affect the afterpeak. We also discuss on the inconsistency of the afterpeak time scale between the simulation and the experiment.

2. Methods

Figure 1 illustrates the experimental setup (identical to the setup in [22]) for the pulsed plasma generation and time-resolved measurement of the plasma emission spectrum. The pulsed plasma is generated by a coaxial transmission line resonator (CTLR). The electric fields of the microwave applied to the CTLR maximize at the end of the electrode, where the working gas stream breaks down and forms a plasma jet. The CTLR used in this study shows an optimal performance at the frequency of 865 MHz, at which maximum microwave power transmission to the plasma occurs. The radio frequency (RF) amplifier amplifies the square microwave pulses generated by the signal generator. The pulse period is varied from 0.4 μs to 32 μs. The duty cycle of the pulse is 50%, and the instantaneous power during on-time is 10 W for all the cases, making the average power to be fixed at 5 W. Additionally, we investigate the plasma driven by continuous power of 5 W as a reference to compare with the pulse-driven cases. Pure argon (Ar) gas (99.9% purity) is injected into the CTLR device as working gas, and the resulting plasma jet spreads into the ambient air. The gas flow rate is 2 standard liters per minute.

We measured the time evolution of the atomic line emissions from the pulsed plasma using a monochromator (Dongwoo 750, 1200 groove mm^{-1}, 500 nm) with an intensified charge-coupled device (ICCD) camera (Princeton, PI-MAX 3). The gating signal for the ICCD camera was fed from the signal generator to ensure synchronized measurements with the pulse cycle. The gate width was fixed at 50 ns, short enough to resolve the plasma evolution during the pulse period. The measurement noise was minimized by accumulating and averaging 1000 shots for each time step. We obtained the time evolution of the spectrum by increasing the gate delay by 50 ns for each time step. To investigate the evolution of the excited species, we focused on the line emission with a wavelength of 750.3 nm from the atomic transition Ar ($3s^2\, 3p^5\, (^2P^o_{1/2})\, 4p$) $\rightarrow$ ($3s^2\, 3p^5\, (^2P^o_{1/2})\, 4s$).

To analyze the mechanism of the plasma afterpeaks, we adopted the COMSOL multiphysics® plasma global model, which evaluates the volume averages of the multitudinous
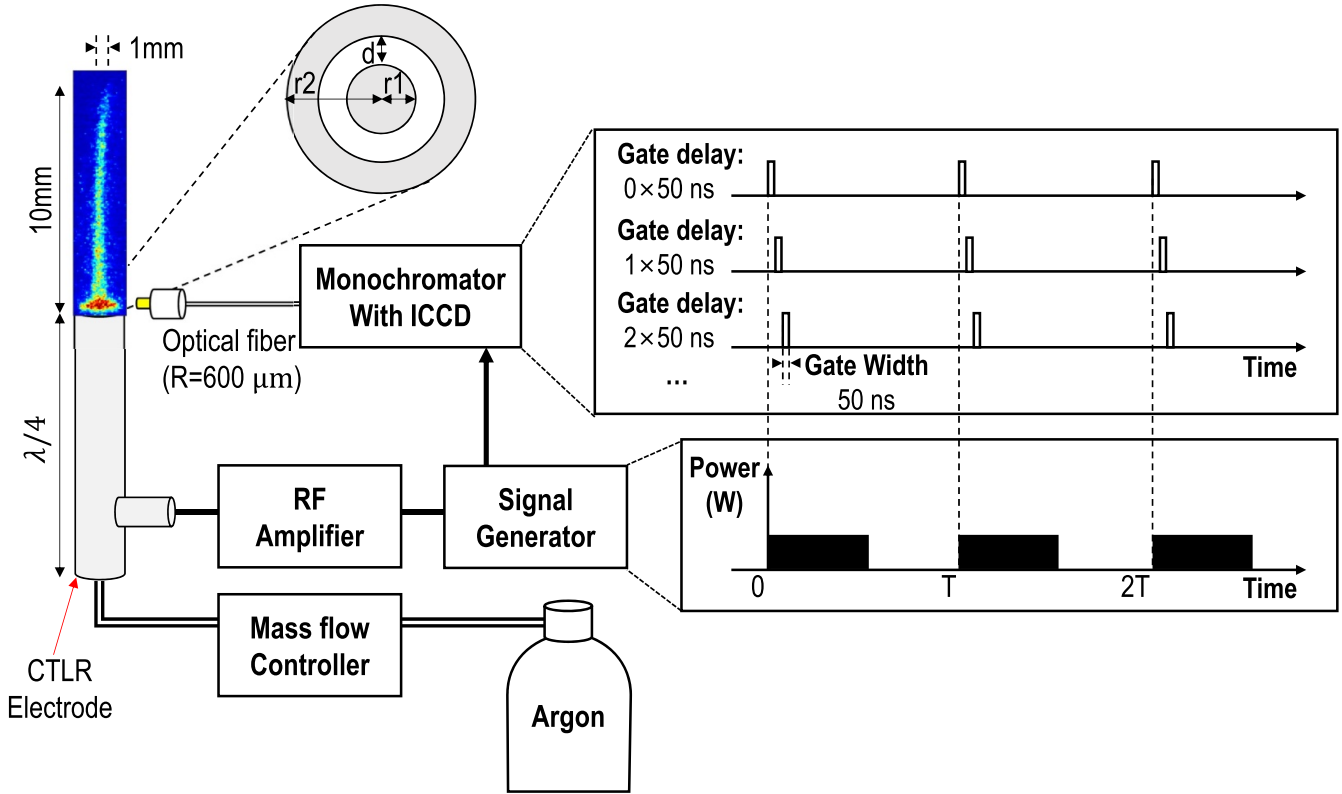
Figure 1. Experimental setup for the operation of the pulsed-microwave CTLR device and the time-resolved spectral measurement of the CTLR plasma jet. The inset diagrams show the periodic microwave pulses and the gating signals for time-resolved spectral measurement. The radius of inner electrode $r_1 = 1.5$ mm, gap $d = 1.5$ mm and the outer radius of outer electrode $r_2 = 3.75$ mm are deigned to match characteristic impedance of electrode to 50 Ω. Reproduced from [22]. © IOP Publishing Ltd. All rights reserved.

chemical reactions and transport processes in the plasma. The global model uses the following particle balance equation to describe the time evolution of each species' density:

$$V\rho\frac{\mathrm{d}w_s}{\mathrm{d}t} = V\sum_{j\epsilon\text{react.}} m_s\Delta_{js}r_j + h_lAR_sm_s - w_sM_0 + M_\text{feed}w_\text{feed,s}$$

(1)

$$M_0 \equiv M_\text{feed} + \sum_{k\epsilon sp.} h_lAR_km_k$$

(2)

where V is the system volume, ρ is the mass density of the gas, w_s is the mass fraction of species s, and m_s is the mass of species s. The first term on the right-hand side corresponds to the net generation or consumption rate of species s by all reactions, where r_j is the rate of the jth reaction per unit volume and Δ_{js} is the number of particles produced by the reaction j. The second term corresponds to the net boundary loss of species s, where R_s is the total boundary particle flux of species s (with the sign convention of negative R_s for net loss), A is the surface area of the plasma and the correction factor h_l is the ratio of the ion density at the sheath edge to the bulk density. h_l is given in chapter 10 of [1] for ion and is unity for neutral species. The boundary particle flux R_k is given by

$$R_k = -n_kv_{k,\text{eff}}$$

(3)

where n_k is the density of the species k. The effective speed $v_{k,\text{eff}}$ depends on the charge of the species k. The effective speed follows the Bohm velocity v_B for ions, whereas it follows the harmonic mean of the zero-wall-density diffusion speed and thermal speed for neutral particles. Details of the effective diffusion speed model have been explained in our previous study [13]. The third term serves to keep the pressure on the simulation volume by replenishing the species s according to the mass fraction w_s and the total mass loss rate M_0 given by equation (2). The fourth term stands for convective input from the gas inlet, where M_feed is the mass flow rate of the feed gas and $w_\text{feed,s}$ is the mass fraction of species s at the feed gas. The convection has little effect in our simulation condition because, during the pulse time scale, the gas jet travels only a few μm, about three orders shorter than the simulation length dimension. To simplify the model, we ignored the convection flow, and set M_feed to zero for this reason.

The following quasi-neutrality condition determines the electron density:

$$0 = -en_e + \sum_s q_sn_s,$$

(4)

where n_s is the density of species s. The electron temperature T_e determines the rate coefficients of electron impact collisions in equation (1), and changes with the electron density (n_e) and electron energy density (n_ε) via the relation $T_e = \frac{2}{3}\frac{n_\varepsilon}{n_e}$. The evolution of n_ε is governed by the energy balance equation:

$$\frac{dn_\varepsilon}{dt} = P_{abs} + \sum_{j\epsilon react.} E_j r_j + \frac{1}{V}\sum_{i\epsilon+ions}(q_i(V_p+V_s)+2T_e)h_l AR_s \tag{5}$$

where V_p is plasma potential and V_s is sheath potential. The first term on the right-hand side of equation (5) corresponds to the absorbed microwave power per unit volume via the Joule heating of the electrons. This term is modeled as a repeating square function to simulate the periodic microwave pulses. The second term is the total electron kinetic energy consumption rate, where E_j is the electron energy loss per the reaction j. The last term corresponds to the power loss per electron and ion escaping at the boundary [2, 24], where the term $q_i(V_p+V_s)$ in the sum represents the kinetic energy of the escaping ions, and the term $2T_e$ represents that of the escaping diffusive electrons assuming isothermal electrons across the sheath. Note that the same number of electrons leave the boundary as the ion escaping assuming charge neutrality. For low voltage sheath and high pressure ($\lambda_i \leq LT_i/T_e$, where λ_i is the ion mean free path, and L is the system size) condition, the plasma and sheath potentials are approximated as follows [2, 25] (note that the temperature is expressed in the unit of voltage):

$$V_p \cong \frac{1}{2}T_e \tag{6}$$

$$V_s \cong \ln\left(4\frac{\overline{u_B}}{v_e}\right)T_e. \tag{7}$$

The global model considers only electrons and argon species as we focus on the root of the plasma jet, where the diffusive mixing of air molecule species is negligible. The heavy Ar species include Ar, Ar(4s), Ar(4p), Ar(3d), Ar(4d), Ar(5p), Ar(5s), Ar(6s), Ar_2^*, Ar^+, and Ar_2^+. Ar_2^* represents the excimer (argon dimer) at the lowest energy state ($A(^3\Sigma_g^+)1_u$). Table 1 lists 91 reactions between the 12 species considered in the global model and their rate coefficients. The Quantemol plasma reaction database provides the reaction constants in the Arrhenius form [26]. The electron impact cross-section data were obtained from the LXCat database [27]. Thermal quenching of higher levels is not included because the reaction rates are negligible compared to spontaneous emission in our condition. The expected gas temperature change during one pulse period is under 1 K, considering the power delivered during one pulse cycle (0.02 mJ) and the heat capacity of the gas in the simulation volume (0.05 mJ K^{-1}). This expectation is indirectly confirmed by time-averaged measurements of OH spectra, showing negligible dependence on the pulse widths. Instead of building a self-consistent thermal equilibrium model to determine the gas temperature for the simulation, the temperature was measured experimentally. The temperature calculated by fitting the rotational spectrum of the OH molecule was constant at 800 K regardless of the pulse period condition. Therefore, the gas temperature was assumed to be constant at 800 K. The simulation geometry of the plasma is a cylinder with a height of 0.4 mm and a radius of 0.4 mm, which corresponds to the observed plasma root volume.

The electron energy distribution function (EEDF) is necessary to calculate the rate coefficients of electron collision reactions using the cross-section data. Since electron-electron collisions are insufficient, the EEDF does not follow the Maxwellian distribution. To calculate the EEDF, we used the two-term Boltzmann equation solver embedded in the COMSOL Multiphysics® plasma module [41]. This solver updates the EEDF in each time step depending on the electron density, electron temperature, densities of the individual species interacting with electrons, and their cross-sections.

The two-term Boltzmann equation is derived from the Legendre polynomial expansion of the distribution function f over $\cos\theta$. Assuming the second-order and higher terms are ignorable, the distribution function f can be approximated as follows:

$$f(v,\cos\theta,z,t) \approx f_0(v,z,t) + f_1(v,z,t)\cos\theta. \tag{8}$$

This approximation is called a two-term approximation. By substituting this approximated distribution function into the Boltzmann equation, multiplying by the 1st and 2nd-order Legendre polynomials, and integrating over $\cos\theta$, the equations for f_0 and f_1 can be obtained. By assuming that

$$f_{0,1}(\varepsilon,z,t) = \frac{1}{2\pi\gamma^3}F_{0,1}(\varepsilon)n(z,t) \tag{9}$$

where $\gamma = (2e/m_e)^{1/2}$ and $\epsilon = (v/\gamma)^2$. The energy dependence can be separated from the dependence on time and space. Following the derivation described in G J M Hagelaar's paper [42], the expressions for $F_{0,1}$ can be rearranged as follows:

$$\frac{\partial}{\partial\varepsilon}\left(W(\varepsilon)F_0(\epsilon) - D(\epsilon)\frac{\partial F_0(\varepsilon)}{\partial\varepsilon}\right) = S \tag{10}$$

$$W(\varepsilon) = -\gamma\varepsilon\sigma_\varepsilon(\epsilon) - 3a\left(\frac{n_e}{N_n}\right)A_1(\varepsilon) \tag{11}$$

$$D(\varepsilon) = \frac{\gamma}{3}\left(\frac{E}{N_n}\right)^2\left(\frac{\varepsilon}{\sigma_\varepsilon(\varepsilon)}\right) + \frac{\gamma k_B T_g}{e}\varepsilon^2\sigma_\varepsilon(\varepsilon)$$
$$+ 2a\left(\frac{n_e}{N_n}\right)\left(A_2(\varepsilon) + \varepsilon^{3/2}A_3(\varepsilon)\right) \tag{12}$$

$$A_1(\varepsilon) = \int_0^\varepsilon u^{1/2}F_0(u)\,du, \quad A_2(\varepsilon) = \int_0^\varepsilon u^{3/2}F_0(u)\,du,$$
$$A_3(\varepsilon) = \int_\varepsilon^\infty F_0(u)\,du \tag{13}$$

$$a = \frac{e^2\gamma}{24\pi\varepsilon_0}\ln\left(\frac{12\pi(\varepsilon_0 k_B T_e)^{3/2}}{e^3 n_e^{1/2}}\right) \tag{14}$$

where $\sigma_\varepsilon(\varepsilon)$ is total elastic cross-section and S is the summation of all inelastic collision operator and normalization factor $R \equiv -\frac{\nu_{ion}}{N}\varepsilon^{1/2}F_0$ (ν_{ion} is ionization collision rate) which ensures that F_0 remains normalized to unity. The solver

Table 1. Reactions included in the global simulation for pure Ar plasma.

#	Equation	A_k	n	E_a	Energy	references
r1	$e + Ar \Rightarrow e + Ar$	$\sigma(\varepsilon)$			*	[28]
r2	$e + Ar \Rightarrow e + Ar(4s)$	$\sigma(\varepsilon)$			11.6	[28]
r3	$e + Ar(4s) \Rightarrow e + Ar$	$\sigma(\varepsilon)$			−11.6	a
r4	$e + Ar \Rightarrow e + Ar(4p)$	$\sigma(\varepsilon)$			13.2	[28]
r5	$e + Ar(4p) \Rightarrow e + Ar$	$\sigma(\varepsilon)$			−13.2	a
r6	$e + Ar \Rightarrow e + Ar(3d)$	$\sigma(\varepsilon)$			14.1	b
r7	$e + Ar(3d) \Rightarrow e + Ar$	$\sigma(\varepsilon)$			−14.1	a
r8	$e + Ar \Rightarrow e + Ar(4d)$	$\sigma(\varepsilon)$			14.8	b
r9	$e + Ar(4d) \Rightarrow e + Ar$	$\sigma(\varepsilon)$			−14.8	a
r10	$e + Ar \Rightarrow e + Ar(5p)$	$\sigma(\varepsilon)$			14.6	[29]
r11	$e + Ar(5p) \Rightarrow e + Ar$	$\sigma(\varepsilon)$			−14.6	a
r12	$e + Ar \Rightarrow e + Ar(5s)$	$\sigma(\varepsilon)$			14.1	b
r13	$e + Ar(5s) \Rightarrow e + Ar$	$\sigma(\varepsilon)$			−14.1	a
r14	$e + Ar \Rightarrow e + Ar(6s)$	$\sigma(\varepsilon)$			14.8	b
r15	$e + Ar(6s) \Rightarrow e + Ar$	$\sigma(\varepsilon)$			−14.8	a
r16	$e + Ar(4s) \Rightarrow e + Ar(4p)$	$\sigma(\varepsilon)$			1.6	b
r17	$e + Ar(4p) \Rightarrow e + Ar(4s)$	$\sigma(\varepsilon)$			−1.6	a
r18	$e + Ar(3d) \Rightarrow e + Ar(5p)$	$\sigma(\varepsilon)$			0.5	b
r19	$e + Ar(5p) \Rightarrow e + Ar(3d)$	$\sigma(\varepsilon)$			−0.5	a
r20	$e + Ar(5p) \Rightarrow e + Ar(4d)$	$\sigma(\varepsilon)$			0.2	b
r21	$e + Ar(4d) \Rightarrow e + Ar(5p)$	$\sigma(\varepsilon)$			−0.2	a
r22	$e + Ar(5p) \Rightarrow e + Ar(6s)$	$\sigma(\varepsilon)$			0.2	b
r23	$e + Ar(6s) \Rightarrow e + Ar(5p)$	$\sigma(\varepsilon)$			−0.2	a
r24	$e + Ar(5s) \Rightarrow e + Ar(5p)$	$\sigma(\varepsilon)$			0.5	b
r25	$e + Ar(5p) \Rightarrow e + Ar(5s)$	$\sigma(\varepsilon)$			−0.5	a
r26	$e + Ar(4p) \Rightarrow e + Ar(3d)$	$\sigma(\varepsilon)$			0.9	b
r27	$e + Ar(3d) \Rightarrow e + Ar(4p)$	$\sigma(\varepsilon)$			−0.9	a
r28	$e + Ar(4p) \Rightarrow e + Ar(4d)$	$\sigma(\varepsilon)$			1.6	b
r29	$e + Ar(4d) \Rightarrow e + Ar(4p)$	$\sigma(\varepsilon)$			−1.6	a
r30	$e + Ar(4p) \Rightarrow e + Ar(5s)$	$\sigma(\varepsilon)$			0.9	b
r31	$e + Ar(5s) \Rightarrow e + Ar(4p)$	$\sigma(\varepsilon)$			−0.9	a
r32	$e + Ar(4p) \Rightarrow e + Ar(6s)$	$\sigma(\varepsilon)$			1.6	b
r33	$e + Ar(6s) \Rightarrow e + Ar(4p)$	$\sigma(\varepsilon)$			−1.6	a
r34	$e + Ar(4s) \Rightarrow e + Ar(5p)$	$\sigma(\varepsilon)$			3	b
r35	$e + Ar(5p) \Rightarrow e + Ar(4s)$	$\sigma(\varepsilon)$			−3	a
r36	$e + Ar \Rightarrow 2e + Ar^+$	$\sigma(\varepsilon)$			15.76	[28]
r37	$e + Ar(4s) \Rightarrow 2e + Ar^+$	$\sigma(\varepsilon)$			4.16	[28]
r38	$e + Ar(4p) \Rightarrow 2e + Ar^+$	$\sigma(\varepsilon)$			2.76	[28]
r39	$e + Ar(3d) \Rightarrow 2e + Ar^+$	$\sigma(\varepsilon)$			1.66	c
r40	$e + Ar(4d) \Rightarrow 2e + Ar^+$	$\sigma(\varepsilon)$			0.96	c
r41	$e + Ar(5p) \Rightarrow 2e + Ar^+$	$\sigma(\varepsilon)$			1.16	c
r42	$e + Ar(5s) \Rightarrow 2e + Ar^+$	$\sigma(\varepsilon)$			1.66	c
r43	$e + Ar(6s) \Rightarrow 2e + Ar^+$	$\sigma(\varepsilon)$			0.96	c
r44	$e + Ar_2^* \Rightarrow 2e + Ar_2^+$	$\sigma(\varepsilon)$			3.8	c
r45	$2e + Ar^+ \Rightarrow e + Ar$	$\sigma(\varepsilon)$			−15.76	d
r46	$2e + Ar^+ \Rightarrow e + Ar(4s)$	$\sigma(\varepsilon)$			−4.16	d
r47	$2e + Ar^+ \Rightarrow e + Ar(4p)$	$\sigma(\varepsilon)$			−2.76	d
r48	$2e + Ar^+ \Rightarrow e + Ar(3d)$	$\sigma(\varepsilon)$			−1.66	d
r49	$2e + Ar^+ \Rightarrow e + Ar(4d)$	$\sigma(\varepsilon)$			−0.96	d
r50	$2e + Ar^+ \Rightarrow e + Ar(5p)$	$\sigma(\varepsilon)$			−1.16	d
r51	$2e + Ar^+ \Rightarrow e + Ar(5s)$	$\sigma(\varepsilon)$			−1.66	d
r52	$2e + Ar^+ \Rightarrow e + Ar(6s)$	$\sigma(\varepsilon)$			−0.96	d
r54	$e + Ar^+ \Rightarrow Ar$	$\sigma(\varepsilon)$			$\frac{3}{2}T_e$	e
r55	$e + Ar^+ \Rightarrow Ar(4s)$	$\sigma(\varepsilon)$			$\frac{3}{2}T_e$	e
r56	$e + Ar^+ \Rightarrow Ar(4p)$	$\sigma(\varepsilon)$			$\frac{3}{2}T_e$	e
r57	$e + Ar^+ \Rightarrow Ar(3d)$	$\sigma(\varepsilon)$			$\frac{3}{2}T_e$	e
r58	$e + Ar^+ \Rightarrow Ar(4d)$	$\sigma(\varepsilon)$			$\frac{3}{2}T_e$	e

(Continued.)

Table 1. (Continued.)

#	Equation	A_k	n	E_a	Energy	references
r59	$e + Ar^+ \Rightarrow Ar(5p)$	$\sigma(\varepsilon)$			$\frac{3}{2}T_e$	e
r60	$e + Ar^+ \Rightarrow Ar(5s)$	$\sigma(\varepsilon)$			$\frac{3}{2}T_e$	e
r61	$e + Ar^+ \Rightarrow Ar(6s)$	$\sigma(\varepsilon)$			$\frac{3}{2}T_e$	e
r62	$e + Ar_2^+ \Rightarrow Ar + Ar(4s)$	6.86×10^{-8}	-0.61		$\frac{3}{2}T_e$	f, [30]
r63	$e + Ar_2^+ \Rightarrow Ar + Ar(4p)$	2.94×10^{-8}	-0.61		$\frac{3}{2}T_e$	f, [30]
r64	$e + Ar_2^+ \Rightarrow e + Ar + Ar^+$	1.36×10^{-6}		2.094	1.5	[26, 31]
r65	$e + Ar_2^* \Rightarrow e + Ar + Ar$	1.00×10^{-9}			-10.5	[26, 32]
r66	$e + Ar + Ar^+ \Rightarrow Ar + Ar(6s)$	1.50×10^{-28}			$\frac{3}{2}T_e$	[26, 33]
r67	$e + Ar + Ar^+ \Rightarrow Ar + Ar(4d)$	1.50×10^{-28}			$\frac{3}{2}T_e$	[26, 33]
r68	$Ar_2^* + Ar_2^* \Rightarrow e + 2Ar + Ar_2^+$	1.00×10^{-9}				[32]
r69	$Ar_2^* \Rightarrow 2Ar$	$6.00 \times 10^{+8}$				[26, 34]
r70	$2Ar + Ar^+ \Rightarrow Ar + Ar_2^+$	2.50×10^{-31}				[26, 34]
r71	$Ar + Ar(4p) \Rightarrow Ar + Ar(4s)$	3.00×10^{-12}				[26, 29]
r72	$Ar + Ar(4s) \Rightarrow Ar + Ar$	2.00×10^{-15}				[26, 29]
r73	$Ar(4s) + Ar_2^* \Rightarrow e + Ar + Ar_2^+$	6.00×10^{-10}	0.5			[26, 35]
r74	$Ar(4s) + Ar(4p) \Rightarrow e + Ar + Ar^+$	5.00×10^{-10}	0.5			[36]
r75	$Ar(4s) + Ar(4s) \Rightarrow e + Ar + Ar^+$	5.00×10^{-10}	0.5			[36]
r76	$Ar(4p) + Ar(4p) \Rightarrow e + Ar + Ar^+$	7.00×10^{-10}	0.5			[36]
r77	$Ar(4s) + Ar(3d) \Rightarrow e + Ar + Ar^+$	7.00×10^{-10}	0.5			[36]
r78	$Ar(4s) + Ar(4d) \Rightarrow e + Ar + Ar^+$	7.00×10^{-10}	0.5			[36]
r79	$Ar(4s) + Ar(5p) \Rightarrow e + Ar + Ar^+$	7.00×10^{-10}	0.5			[36]
r80	$Ar(4s) + Ar(5s) \Rightarrow e + Ar + Ar^+$	7.00×10^{-10}	0.5			[36]
r81	$Ar(4s) + Ar(6s) \Rightarrow e + Ar + Ar^+$	7.00×10^{-10}	0.5			[36]
r82	$Ar(4s) + Ar(4s) \Rightarrow e + Ar_2^+$	6.30×10^{-10}	-0.5			[26, 33]
r83	$Ar(4p) \Rightarrow Ar(4s)$	$3.76 \times 10^{+8} \cdot \eta$				g, [37]
r84	$Ar(5p) \Rightarrow Ar(4s)$	$1.65 \times 10^{+7} \cdot \eta$				g, [37]
r85	$Ar(3d) \Rightarrow Ar(4p)$	$1.46 \times 10^{+8} \cdot \eta$				g, [37]
r86	$Ar(5s) \Rightarrow Ar(4p)$	$8.81 \times 10^{+7} \cdot \eta$				g, [37]
r87	$Ar(4d) \Rightarrow Ar(4p)$	$2.70 \times 10^{+7} \cdot \eta$				g, [37]
r88	$Ar(6s) \Rightarrow Ar(4p)$	$1.78 \times 10^{+8} \cdot \eta$				g, [37]
r89	$Ar(5p) \Rightarrow Ar(3d)$	$1.38 \times 10^{+6} \cdot \eta$				g, [37]
r90	$Ar(5p) \Rightarrow Ar(5s)$	$3.15 \times 10^{+7} \cdot \eta$				g, [37]
r91	$Ar(4d) \Rightarrow Ar(5p)$	$2.80 \times 10^{+7} \cdot \eta$				g, [37]
r92	$Ar(6s) \Rightarrow Ar(5p)$	$1.68 \times 10^{+7} \cdot \eta$				g, [37]

For reactions 1–61, indicated by $\sigma(\varepsilon)$, the reaction rate is determined using the two-term Boltzmann equation solver and cross-section data. The rates coefficient of reactions 62–92 are given in the Arrhenius form: $k = A_k \cdot (T)^n \exp\left(-\frac{E_a}{T}\right)$. The unit of A_k is s^{-1}, $cm^3\,s^{-1}$, and $cm^6\,s^{-1}$ for the first, second, and third-order reactions, respectively. The unit of temperature T is K for heavy particle reactions and eV for electron collision reactions. The unit of E_a is the same as that of T.

*The electron energy loss by elastic collision is given by $m_r \cdot 3(T_g - T_e)$, where m_r is mass fraction of electron and argon.

a The cross-section is calculated under the principle of detailed balance using corresponding excitation cross-section data [38].

b Empirical cross-section of electron impact excitation taken from [29, 37].

c Empirical cross-section of electron impact ionization taken from [29, 37].

d The cross-section is calculated under the principle of detailed balance, considering it as the inverse reaction of electron impact ionization [38].

e The cross-section is calculated under the principle of detailed balance, considering it as the inverse reaction of photo-ionization. The cross-section of photo-ionization is taken from [29].

f The dissociative recombination coefficients are calculated based on the known reaction coefficient $9 \times 10^8 \cdot (T_e)^{-0.61}$ [30] assuming the ratio of Ar(4s) to Ar(4p) production is 3:7 [39].

g These reactions correspond to the net spontaneous transition considering RT. The so-called escape factor η is calculated using the formula introduced in [40]. The escape factor η in each reaction equation is calculated independently.

calculates the value of reduced electric field E/N_n that satisfies $n_\varepsilon/n_e = \int_0^\infty \varepsilon F_0(\varepsilon)\,d\varepsilon$ using the finite element method.

We also considered the RT of spontaneous emission. When the lower level of spontaneous decay is dense enough, the emitted radiation is reabsorbed before escaping the plasma volume. This process occurs sequentially so that a portion of the radiation is trapped in the plasma volume. This phenomenon is called RT. The effect of RT is expressed by multiplying the escape factor η to the corresponding Einstein coefficient A_r. The escape factor η depends on the plasma size and absorption coefficient k_0 [39]:

$$k_0 = n_l A_r \frac{g_h}{g_l} \frac{\lambda^3}{8\pi^{3/2}} \frac{1}{v_0} \tag{15}$$

where, n_l is the density of low energy level, λ is the wavelength of the radiation, $g_{h,l}$ are statistical weights, and v_0 is the

thermal velocity of the atom. There are several different approaches to calculating the escape factor. We adopted the formula of Mills and Hieftje [39]

$$\eta = g_0 \left(T_D \exp\left(-\frac{\pi T_{CD}^2}{4T_C^2} \right) + T_C \operatorname{erf}\left(\frac{\pi^{1/2} T_{CD}}{2T_C} \right) \right) \quad (16)$$

where g_0 is a constant depending on the absorption profile and trap geometry. The dimensionless parameters T_D, T_C, and T_{CD} are

$$T_D = \frac{1}{k_0 \rho (\pi \ln k_0 \rho)^{1/2}}, \ T_C = \left(\frac{b}{\pi^{1/2} k_0 \rho} \right)^{1/2},$$

$$T_{CD} = \frac{2b}{\pi (\ln k_0 \rho)^{1/2}} \quad (17)$$

where $b = (A_r + \nu_c) \lambda / (4\pi \nu_0)$ and ρ is the characteristic length of plasma. In a cylindrical geometry, g_0 is 1.9 for the profile dominated by Doppler-broadening and 1.3 for the profile dominated by pressure broadening. Because the pressure broadening dominates the absorption profile in the atmospheric pressure condition, we set $g_0 = 1.3$. ν_c is collision frequency between atoms. We assume the radius of the collision cross-section is the van-der-Waals radius of argon. Since our model did not deal with the detailed levels of argon, it was calculated assuming that the levels of each term (four levels of Ar(4s), ten levels of Ar(4p), etc) have the same population. The η value of emission generated when the resonant state of Ar(4s) transitions to the ground state is about 10^{-4} under an atmospheric pressure environment. In our experimental condition, the transition loss was comparable to the consumption by diffusion, so the transition of Ar(4s) to ground state was not considered in the simulation.

The falling time of the measured input microwave signal is about 10 ns. Note that this falling time is not of the dissipated power but of the signal generator. Since the inductance of our electrode is negligibly small, we assumed that the time scale of dissipated power is the same as that of the input signal.

We ran each simulation until the plasma reached a periodic steady state. The pulse period was varied between 0.4–32 μs as in the experiment, and the rising time and falling time was fixed to 10 ns. The time-averaged dissipated power was set to 5 W, which is the same with experimental condition. The steady-state values of the plasma properties were used in the following analysis.

3. Results and discussion

3.1. Experimental result on varying pulse periods

Our experiments show that a proper pulse condition (pulse duration and period) can substantially enhance the production of excited states at a given time-averaged power input, which is reproduced by global modeling. We observe the evolution of the 750.3 nm line emission for various pulse periods (figure 2(a)). This line emission corresponds to the spontaneous transition from Ar $(^2P^o_{1/2})$ 4p to $(^2P^o_{1/2})$ 4s. The line intensity is proportional to the density of the upper state $(^2P^o_{1/2})$

4p. In figure 2(a), the time axis is normalized by the period of each case for comparison. The results show a rapid increase in the line emission after turning the pulse power on and off. The emission burst observed at the pulse-on time has been attributed to the increase of T_e [1, 13]. This emission burst at the pulse-on is called prepeak [18]. Another substantial increase in the emission after pulse-off is called the afterpeak. The afterpeak phenomena have been reported in a variety of low-pressure plasmas [18–23] with a qualitative picture of the underlying mechanism: a rapid decrease of T_e in the afterglow phase amplifies Ar dimer ions' recombination reaction, which generates the excited Ar atoms.

Our experiments show that the time-averaged emission from the pulsed plasma can become more intense than that of the CW plasma due to the afterpeak and prepeak under the same average power condition. Figure 2(b) compares the time-averaged 750.3 nm line emissions for various pulse periods normalized by the intensity of the CW case. The averaged emission intensity, which peaks around the pulse period of 1 μs, converges to the CW emission intensity as the pulse period decreases. When the pulse period is shorter than the prepeak and afterpeak time scales, the input power switches its phase before T_e and n_e change sufficiently, resulting in a lesser variation in the emission intensity, and the characteristics of the pulsed operation disappear.

In contrast, as the pulse period increases from the peak of averaged emission intensity, it converges to half the CW intensity. In the long pulse period limit, the time scales of the prepeak and afterpeaks become independent of the pulse period because they only depend on the plasma states immediately before the power on/off. In addition, the emission intensity during the pulse-on time approaches the CW intensity level despite different instantaneous power densities, while the inter-pulse time yields approximately no emission. Thus, the emission intensity in a long period pulse condition approximately follows the modulation of the input pulse power, so the average intensity converges to the CW intensity times the duty cycle. The duty cycle was 50%, so the averaged emission intensity converges to half of CW intensity.

One can maximize the time-averaged emission by turning on the pulse power at the moment when the afterglow emission intensity reaches its maximum value. Figure 2(b) shows the pulsed operation that increases the time-averaged emission intensity up to 220% of the CW case. Since the line emission intensity is proportional to the density of the corresponding Ar excited state, this condition is equivalent to maximizing the population density of the excited state. To maximize the time-averaged emission, the proportions of afterpeak and prepeak during one period should be maximized. We can achieve the maximization by adjusting the next pulse when the afterpeak starts to decrease.

3.2. Global simulation to reproduce the afterpeak

We attempted to simulate the afterpeak phenomenon at atmospheric pressure using a global model. In this process, we found that the HLs and RT are essential for the reproduction of afterpeak. Global models in general aim to capture the
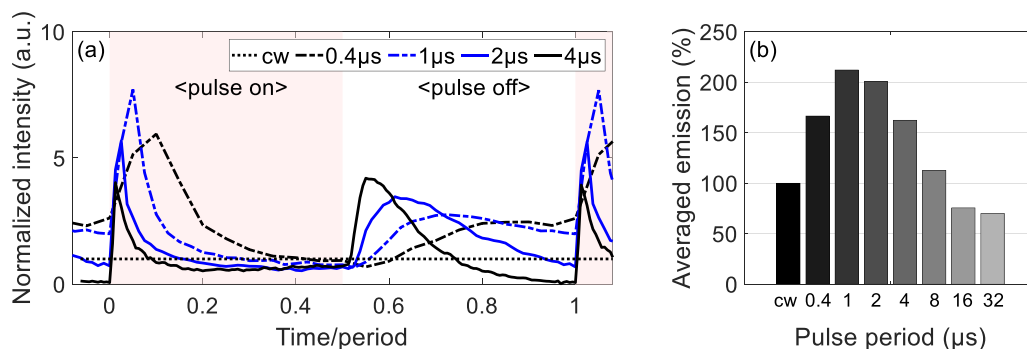
Figure 2. (a) Time evolution of the experimental measurement of 750.3 nm line emission and (b) time average of 750.3 nm line emission for varying pulse periods.

main pathways of energy and particle transport and predict the parametric dependence or trend of radical species generation. Global models attain high calculation speed by simplifying the very complex network of chemistry and atomic processes in plasma into a manageable set of reaction equations. For instance, global models for argon plasmas usually consider only the atomic levels of 4p and below because the argons with HLs are low in density and so the radical generations by them would be minimal. As for the RT, which is an important process in atmospheric pressure plasmas, global models usually consider only the transitions with the ground state as the lower level, such as the transition from the argon ground state to the 4s states. This is because the RT by reabsorption of spontaneous emission requires a high density of the corresponding lower level. However, our study shows that HLs and the RT by excited species are essential ingredients in simulation for reproducing the afterpeak phenomena.

Figure 3 shows the simulation results on whether the model considers HLs and RT. Other conditions such as plasma size, average power, pressure, and gas temperature were kept constant. The model without HL considers only 33 reactions and seven species, excluding 59 reactions involving high energy levels. The model without RT assumes the escape factor of unity. Figure 3 shows the plot of the time evolution of the spontaneous transition from Ar(4p) to Ar(4s), which corresponds to the 750.2 nm line emission in figure 2. The experimental result clearly shows the afterpeak of the corresponding line emission, but in the simulation, the afterpeak occurs only in the model considering both HL and RT. This result implies that these two physical phenomena significantly affect the afterpeak occurrence.

We tried to predict the average emission according to the various periods, as shown in figure 2, using a model that considers both HL and RT. Because the afterpeak timescales of the experiments and simulations were different, the periods plotted in figure 4(a) were chosen to have a shape similar to figure 2(a). Although the afterpeak time scale in simulation is much shorter than the actual time scale, our model can reproduce the phenomena such as afterpeak and prepeak. When the period is much shorter compared to the timescale of afterpeak, the average transition converges to the same as in the case of CW, and when the period is too long, it converges to half of CW. Note that this tendency is the same as the experiment
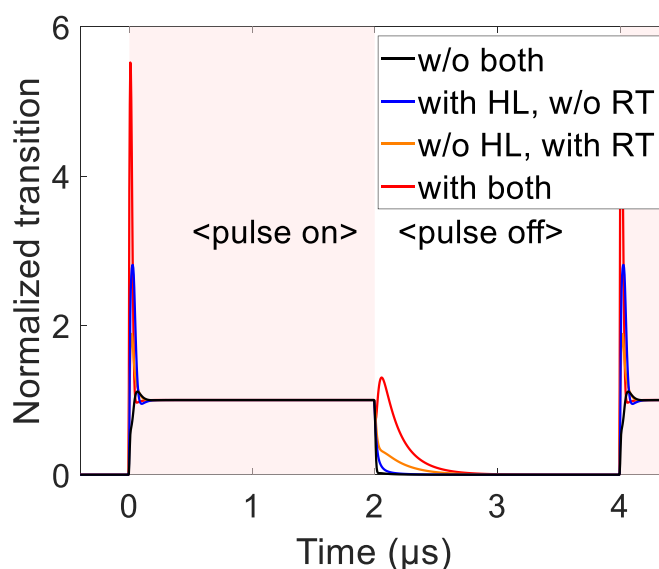

Figure 3. Comparison of time evolution of normalized net spontaneous transition from Ar(4p) to Ar(4s) with and without highly excited levels and radiation trapping (r83 in table 1). The pulse period is 4 μs. The emission rate is normalized by steady state emission rate.

result. The experiment's emission evolution characteristics are also shown in the simulation: (a) the emission intensity during the pulse-on time converges to the emission intensity of CW, and (b) the timescales of prepeak and afterpeak are almost constant regardless of period. Because the characteristics of emission evolution are the same, we can apply the same analysis as in section 3.1 to the simulation results. The time-averaged emission shown in figure 4(b) can also be maximized by adjusting the pulse period with respect to the timing of the afterpeak.

3.3. Mechanism of the prepeak and afterpeak

Figure 5 shows the overall evolution of the reactive Ar species densities (except for the ground state Ar) for the case of 4 μs pulse period. The density variation of the ground state Ar is negligible due to its high density and low ionization order. Note that significant amounts of Ar dimer ions are
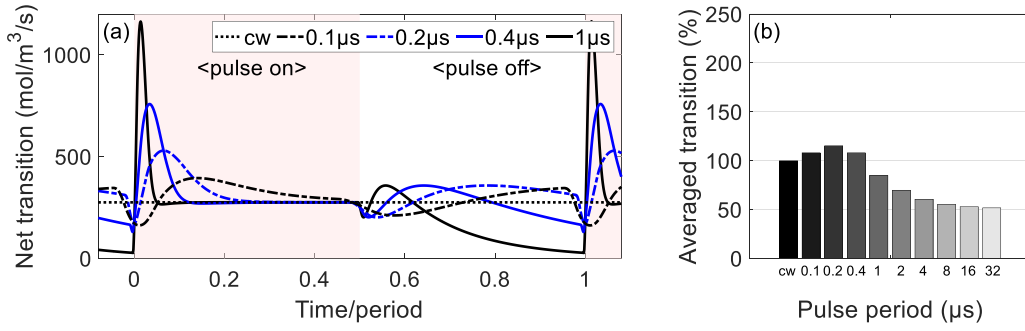
Figure 4. (a) Net spontaneous transition rate from Ar(4p) to Ar(4s) (r83 in table 1) within one pulse cycle for varying pulse periods in the global simulation. Note that the net spontaneous transition rate means the transition rate reduced by radiation trapping. The horizontal time axis is normalized by each period. (b) Time-averaged transition rates normalized by the rate of CW case for varying pulse periods.
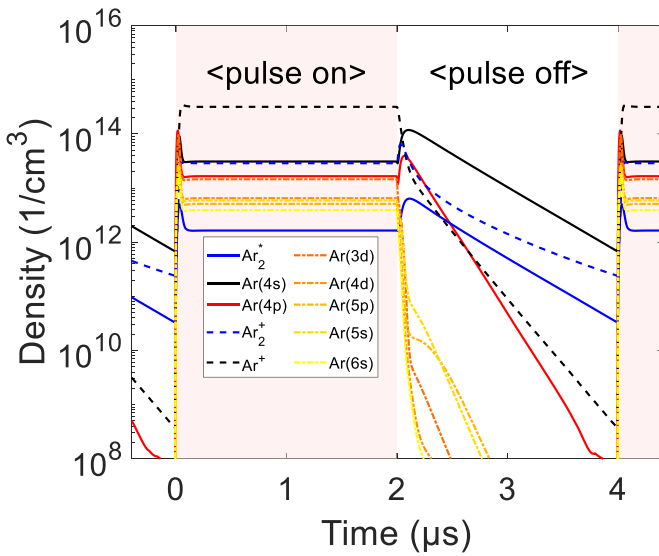
Figure 5. Density evolution of excited species and ions in the global model simulation. The pulse period is 4 μs.

present because the atmospheric pressure condition enhances the three-body attachment reactions (r25–r27 of table 1), turning Ar atomic ions into Ar dimer ions.

Figure 6(a) shows the time evolution of T_e and n_e, which are essential to explain the mechanism of the prepeak and afterpeak. We divided the pulse period into several stages to examine the prepeak and afterpeak processes closely. The numbers at the top of the figure indicate the stages of plasma evolution selected for ease of explanation. At stage 1 (the pulse-on moment), the external power heats the low-density electrons until the electrons gain enough energy and the subsequent collisional energy losses become significant. This initial heating of electrons rapidly increases T_e with the time scale τ_{on}

$$\frac{1}{\tau_{\text{on}}} \equiv \frac{1}{T_e}\frac{\mathrm{d}T_e}{\mathrm{d}t} \approx \frac{1}{n_\epsilon}\frac{\mathrm{d}n_\epsilon}{\mathrm{d}t} \approx \frac{P_{\text{abs}}}{n_\epsilon} \qquad (18)$$

In the simulation, P_{abs} is approximately $2.5 \times 10^{26}\,\text{eV}\,(\text{m}^3\,\text{s})^{-1}$ and n_ϵ is about $1 \times 10^6\,\text{eV}\,\text{m}^{-3}$ at the moment of pulse-on, yielding sub-ns scale τ_{on}.

T_e and n_ϵ would reach a momentary equilibrium as the electron energy loss reactions become significant and balance with the external power absorption (the end of stage 1):

$$P_{\text{abs}} \approx -\sum_{j\epsilon\text{react.}} E_j r_j - \frac{1}{V}\sum_{i\epsilon+\text{ions}} (q_i\,(V_p + V_S) + 2T_e)h_l AR_S. \qquad (19)$$

In stage 2, T_e decreases as electron-impact ionization and other loss channels increase with electron density. In stage 3 (assuming that the pulse length is long enough), a steady-state is reached, constrained by the power balance equation (19) and all the density balance equations.

Stage 4 corresponds to the very short time window after the external power is turned off ($P_{\text{abs,off}} = 0$). In this stage, T_e drops rapidly, and the collisional excitation of the ground state Ar becomes negligible. In stage 5, the electron energy density decreases with the time scale τ_{off} determined as follows:

$$\frac{1}{\tau_{\varepsilon,\text{off}}} \equiv \frac{1}{n_\varepsilon}\frac{\mathrm{d}n_\varepsilon}{\mathrm{d}t} = \frac{1}{n_\varepsilon}\left(-\sum_{j\epsilon\text{react.}} E_j r_j - \frac{1}{V}\sum_{i\epsilon+\text{ions}}\right.$$
$$\left. \times (q_i(V_p + V_s) + 2T_e)h_l AR_S\right) \approx \frac{P_{\text{abs,on}}}{n_\varepsilon}. \qquad (20)$$

In our simulation, the steady-state n_ε during the pulse-on time is approximately $10^{19}\,\text{eV}\,\text{m}^{-3}$ yielding $\tau_{\text{off}} \sim 0.04\,\mu\text{s}$. T_e decreases to 0.4 eV in a similar time scale while n_e decreases relatively slowly.

In stages 6 and 7, which correspond to low T_e below 1 eV, the electron loss becomes dominant, reducing the electron impact ionization, hence n_e decreases with the time scale $\tau_{e,\text{off}}$:

$$\frac{1}{\tau_{e,\text{off}}} \equiv \frac{1}{n_e}\frac{\mathrm{d}n_e}{\mathrm{d}t} \approx \frac{r_{\text{rec}} + r_{\text{diff}}}{n_e}, \qquad (21)$$

where r_{rec} (r_{diff}) is the rate of electron loss by recombination (diffusion). In our simulation condition, $\tau_{e,\text{off}} \geq 1\,\mu\text{s} \gg \tau_{\varepsilon,\text{off}}$ and it will be valid for most cold plasma.

The evolution of Ar(4p) density can be understood along with the changes of n_e and T_e. In stages 6 and 7, the afterpeak occurs due to the low T_e, which breaks the balance between the production and consumption of the excited argon species. As
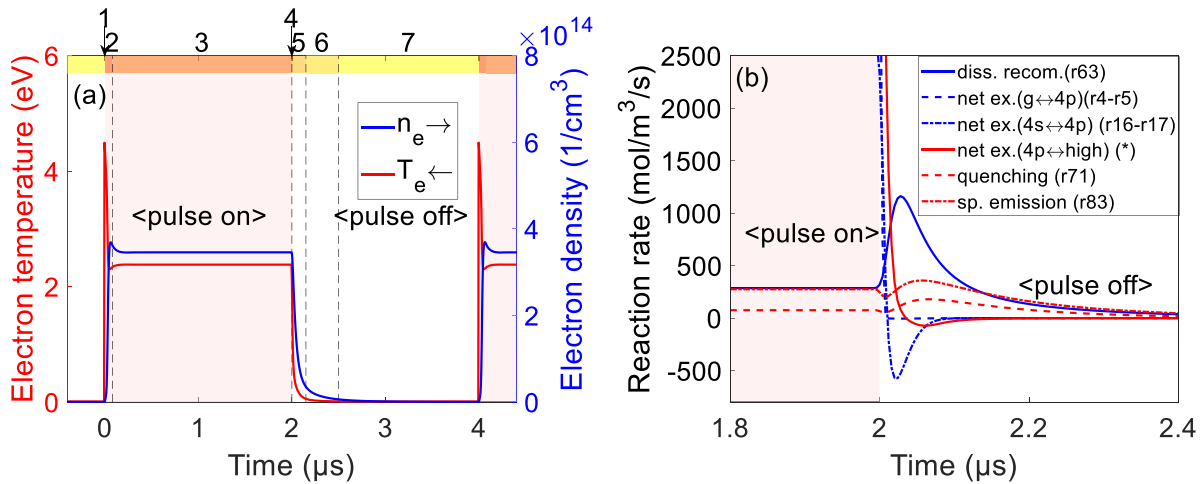
Figure 6. (a) Time evolution of the electron temperature and density and (b) time evolution of dominant generation (blue) and loss (red) processes of Ar(4p). Net excitations mean the excitation rate minus the de-excitation rate. In the inset box, 'high' indicates all levels higher than 4p. Note that the net excitation from 4p to higher level is loss channel of Ar(4p).

T_e decreases, collisional excitation vanishes. The more energy required for excitation, the faster the reaction rate decreases. On the other hand, the reaction rates of recombination are enhanced at low T_e.

Figure 6(b) compares the reaction rate of the key reactions. Ar(4p) density decreases slightly in stage 4 because the excitation from the ground state to Ar(4p) vanishes most rapidly (this excitation requires 13.2 eV). Then, in stages 5 and 6, the afterpeak begins due to reducing the excitation to higher levels and enhancing the recombination reactions. The excitations to higher levels are the dominant loss channel of Ar(4p). Among the recombination reactions, only the dissociative recombination of argon dimer ion is significant. In addition, the de-excitation rate from higher energy level exceeds the excitation rate while the ionizations of high energy levels are rapidly reduced. Thereafter, spontaneous emission (r83) dominates the relaxation of Ar(4p), which determines the time scale of afterpeak.

3.4. Discussion on modeling for the afterpeak

The HLs act as energy steps, enhancing the ionization efficiency. The energy level difference between the high levels is approximately 1 eV so that excitation can occur easily by collisions with low energy electrons. The process in which ionization occurs from a high level generated by such sequential excitation is called multistep ionization. In the steady-state of pulse on time, the ionization from high energy levels accounts for 75% of the total ionization. In a model ignoring the high levels, multistep ionization cannot occur and therefore the electron and ion densities are underestimated while the Ar(4p) density are overestimated due to the absence of the loss channel related to the multistep ionization. Decreasing the density of electrons and ions reduces the recombination rate, and increasing Ar(4p) enhances the rate of most of Ar(4p) consumption reactions. In models considering high energy levels, the dominant consumption of Ar(4p) species at a steady state

is net excitation to high levels, which is rapidly reduced in the afterglow phase due to low electron temperature. In models that ignore high energy levels, on the other hand, the dominant consumption reaction is quenching. Since this reaction is not affected by the electron temperature, it causes considerable consumption even in the afterglow phase, which makes the model fail to reproduce the afterpeak.

RT prevents rapid decay of excited argon in the afterglow, allowing the emissions to remain for longer. Without considering RT, the spontaneous transition time of Ar(4p) to Ar(4s) is tens of nanoseconds. According to the simulation results, the absorption length (inverse of the absorption coefficient k_0) of this emission is approximately 10 μm, which is much shorter than the plasma size in our experiment and simulation of atmospheric pressure plasma. The escape factor η corresponding to the experimental condition is estimated to be approximately 0.02. Thus, if a model ignores RT effect, it will overestimate the radiational loss by a factor of 50 or more. Contrary to the more familiar case of low-pressure plasma, the density of Ar(4s) in atmospheric pressure argon plasma is sufficiently high, which effectively suppresses the spontaneous transition from Ar(4p) to Ar(4s) via RT. In other words, the models that ignore RT will underestimate the density of Ar(4p).

The simulation timescale is shorter than the experimental one because our model underestimates the RT volume of the plasma. The global model assumes uniform power over the entire plasma, but the power will be transmitted intensively to the plasma root in the experiment. Our model adjusted the power transfer density to be similar to the experimental situation by taking only the plasma root as the plasma volume. However, visible camera imaging of the CTLR plasma suggests that the plasma dimension relevant to the RT is ~20 mm, much larger than the dimension of the plasma root (~0.4 mm). This inconsistency makes the model overestimate the radiational loss and underestimate the afterpeak time scale. To solve this inconsistency, future work will adopt a model

considering the non-uniform spatial distribution of species densities.

4. Conclusion

We studied the afterpeaks generated in the pulsed microwave operation of an atmospheric pressure plasma. The global simulation was performed under the same conditions as the experiment, and the simulation results were compared with the experimental measurements. Although the simulation underestimated the time scale, the trends with the pulse operation parameters were consistent with the experimental observations where the time scales of the prepeak and afterpeak phenomena were of the order of 1 μs. By adjusting the pulse operation parameters concerning the afterpeak time scale, we demonstrated that the time-averaged density of Ar(p) can increase by more than 200% compared to the CW operation. To maximize the average density, the next pulse began at the time when the afterpeak intensity reached the maximum. This scheme can be applied to atmospheric pressure Ar plasmas and various gas and discharge conditions where afterpeak occurs. We conclude that the time scale of afterpeak is a key factor in such optimization strategy.

To clarify the afterpeak mechanism, we analyzed the global simulation results and investigated the key reaction and the time scale of plasma properties. In power-on duration, the density of Ar(p) reached a steady-state value balanced by consumption (primarily due to ionization) and generation (due to excitation reactions). When the power was turned off (at the beginning of inter-pulse time or afterglow), T_e decreased rapidly due to energy consumption by electron collision reactions. Because the time scale of n_e is much longer than that of T_e, the plasma transiently has high n_e and low T_e. The density of Ar(4p) starts to increase because the low T_e condition reduces the excitations to higher levels and enhances the recombination reactions. In terms of energy transfer, the low T_e of the afterglow phase prevents the energy release by diffusion, exciation, and ionization. Instead of the stored energy being consumed by those channels, the energy decays into the excited species by the enhanced recombination reaction. A similar mechanism may apply to other afterpeak phenomena with different discharge conditions.

Our work has shown that the afterpeak phenomenon cannot be reproduced without considering high energy level argon species and RT of transition between excited levels, which are not considered in general global models. Without considering high energy levels, the ionization order is underestimated and the generation of Ar(4p) by recombination at inter-pulse time is reduced. In models that ignore RT, Ar(4p) 's radiational loss rate is so fast that Ar(4p) cannot remain longer than 1 μs. These results suggest that high energy level argon and RT must be considered when building high-dimensional simulations to precisely reproduce the afterpeak phenomenon. Global simulations that do not consider these may underestimate the densities of reactive species in the plasma. In particular, the effect of RT is significant for atmospheric pressure plasma, and consideration of the emission reabsorption is essential.

ORCID iDs

Seokyong Jeong ⓘ https://orcid.org/0000-0002-4311-1195
Woojin Nam ⓘ https://orcid.org/0000-0002-2124-4122
Gunsu Yun ⓘ https://orcid.org/0000-0002-1880-5865

References

[1] Lieberman M A and Lichtenberg A J 2005 *Principles of Plasma Discharges and Materials Processing* 2nd edn (New York: Wiley)
[2] Krasikc Y E, Yarmolich D, Gleizer J Z, Vekselman V, Hadas Y, Gurovich V T and Felsteiner J 2009 *Phys. Plasmas* **16** 057103
[3] Bokhan P A, Zakrevsky D E and Gugin P P 2011 *Phys. Plasmas* **18** 103112
[4] Pearlman J S and Riordan J C 1981 *J. Vac. Sci. Technol.* **19** 1190
[5] Harrison W W, Hess K R, Marcus R K and King F L 1986 *Anal. Chem.* **58** 341–56
[6] Hoffmann V, Kasik M, Robinson P K and Venzago C 2005 *Anal. Bioanal. Chem.* **381** 173–88
[7] Lee M U, Lee J K and Yun G S 2018 *Plasma Process. Polym.* **15** 1700124
[8] Rousseau A, Tomasini L, Gousset G, Boisse-Laporte C and Leprince P 1994 *J. Phys. D: Appl. Phys.* **27** 2439
[9] Baeva M, Gier H, Pott A, Uhlenbusch J, Höschele J and Steinwandel J 2001 *Plasma Sources Sci. Technol.* **11** 1
[10] Rousseau A, Dantier A, Gatilova L, Ionikh L, Röpcke J and Tolmachev Y 2005 *Plasma Sources Sci. Technol.* **14** 70
[11] Laimer J, Shimokawa M and Matsumoto S 1994 *Diam. Relat. Mater.* **3** 231–8
[12] Economou D J 2014 *J. Phys. D: Appl. Phys.* **47** 303001
[13] Jeong S Y, Nam W J, Lee J K and Yun G S 2018 *J. Phys. D: Appl. Phys.* **51** 454001
[14] Ferguson E E 1992 *J. Am. Soc. Mass Spectrom.* **3** 479–86
[15] Benedictis S and Dilecce G 2002 *Pure Appl. Chem.* **74** 317–26
[16] Chou C and Phillips J 1992 *J. Mater. Res.* **7** 2107–13
[17] Martirosyan A E, Altucci C, Bruno A, de Lisio C, Porzio A and Solimeno S 2004 *J. Appl. Phys.* **96** 5450
[18] Klinger J A, Savickas P J and Harrison W W 1990 *J. Am. Soc. Mass Spectrom.* **1** 138–43
[19] Yan X, Lin Y, Huang R, Hang W and Harrison W W 2010 *J. Anal. At. Spectrom.* **25** 534–43
[20] Carbone E, Sadeghi N, Vos E, Hübner S, van Veldhuizen E, van Dijk J, Nijdam S and Kroesen G 2015 *Plasma Sources Sci. Technol.* **24** 015015

[21] Chaplin V H and Bellan P M 2016 *Phys. Plasmas* **23** 083506
[22] Nam W J, Jeong S Y, Lee J K and Yun G S 2018 *J. Phys. D: Appl. Phys.* **51** 444001
[23] Bogaerts A 2007 *J. Anal. At. Spectrom.* **22** 502–12
[24] Ashida S, Lee C and Lieberman M A 1995 *J. Vac. Sci. Technol.* B **13** 2498
[25] Thorsteinsson E G and Gudmundsson J T 2010 *Plasma Sources Sci. Technol.* **19** 015001
[26] Jonathan T *et al* 2017 QDB: a new database of plasma chemistries and reactions *Plasma Sources Sci. Technol.* **26** 055014
[27] LXCat team Plasma Data Exchange Project (available at: www.lxcat.net) (Accessed 25 August 2020)
[28] Biagi S F Fortran program, MAGBOLTZ Biagi-v7.1 database (available at: www.lxcat.net) (Accessed 8 November 2021)
[29] Vlcek J 1989 *J. Phys. D: Appl. Phys.* **22** 623
[30] Shiu Y-J and Biondi M A 1978 *Phys. Rev.* A **17** 868
[31] Bultel A, van Ootegem B, Bourdon A and Vervisch P 2002 *Phys. Rev.* E **65** 046406
[32] Lorents D C 1976 *Physica* B+C **82** 19–26

[33] Kang N, Gaboriau F, Oh S-G and Ricard A 2011 *Plasma Sources Sci. Technol.* **20** 035002
[34] Kannari F, Suda A, Obara M and Fujioka T 1983 *IEEE J. Quantum Electron.* **19** 1587–600
[35] Lam S K, Zheng C-E, Lo D, Dem'yanov A and Napartovich A P 2000 *J. Phys. D: Appl. Phys.* **33** 242
[36] Rolin M N, Shabunya S I, Rostaing J C and Perrin J M 2007 *Plasma Sources Sci. Technol.* **16** 480
[37] Petrov G M and Ferreira C M 2013 arXiv:1308.2593
[38] Bogaerts A, Gijbels R and Vlcek J 1998 *J. Appl. Phys.* **84** 121–36
[39] Royal J and Orel A E 2006 *Phys. Rev.* A **73** 042706
[40] Mills J W and Hieftje G M 1984 *Spectrochim. Acta* B **39** 859–66
[41] COMSOL, Inc. 2020 COMSOL multiphysics reference manual (version 5.5) (available at: www.comsol.com) (Accessed 10 September 2020)
[42] Hagelaar G J M and Pitchford L C 2005 *Plasma Sources Sci. Technol.* **14** 722